Full length article

Quantitative study of the effect of grain boundary parameters on the slip system level Hall-Petch slope for basal slip system in Mg-4Al

Mohsen Taheri Andani [a,b,*], Aaditya Lakshmanan [c], Veera Sundararaghavan [b,c], John Allison [b], Amit Misra [a,b]

[a] Department of Mechanical Engineering, University of Michigan, Ann Arbor, MI, United States
[b] Department of Materials Science and Engineering, University of Michigan, Ann Arbor, MI, United States
[c] Department of Aerospace Engineering, University of Michigan, Ann Arbor, MI, United States

ABSTRACT

Several theoretical studies have reported that the geometry and structure of grain boundaries in polycrystalline materials could impose a significant effect on the Hall-Petch slope. However, experimental observations are primarily limited by the ability of the techniques to accurately quantify the grain boundary strength and validate these theoretical models. Using high-resolution electron backscatter diffraction (HR-EBSD), the local stress tensor ahead of a slip band blocked by a grain boundary was quantified and coupled with a continuum dislocation pile-up model to assess the barrier strength of specific grain boundaries to specific slip systems, referred to as micro-Hall-Petch coefficient. For basal slip system in a deformed Mg-4Al alloy, the micro-Hall-Petch coefficient (k_μ^{basal}) varied significantly, from 0.054 to 0.184 MPa $-$ m$^{1/2}$ for nine different grain boundaries. These results were correlated with geometric descriptors of the respective grain boundaries, with three-dimensional GB profile additionally measured via focused ion beam milling. It was found that the angle between the two slip plane traces on the grain boundary plane was the most sensitive parameter affecting k_μ^{basal}, followed by the angle between the slip directions. A functional form for calculation of k_μ^{basal} depending on these two angles is proposed to augment crystal plasticity constitutive models with slip resistance dependent on some measure of the grain size. The method allows a new pathway to calibrate grain size strengthening parameters in crystal plasticity models, allowing further computational investigations of the interrelationship between texture, grain morphology, and the Hall Petch effect.

1. Introduction

Magnesium (Mg) alloys, owing to their low density, which is 23% that of steel and 66% that of aluminum [1,2], continue to receive significant attention for weight-saving applications. However, the widespread industrial application of Mg alloys is hindered by their low strength and limited room temperature formability. Several strategies have been proposed to improve the strength and formability of Mg alloys include solid solution alloying [3–5], precipitate hardening [6–8], grain refinement [9,10], and basal texture weakening [11–13]. Among these techniques, grain refinement is one of the most common techniques used to improve the yield strength of Mg alloys according to the well-known Hall-Petch equation [14–17], which connects the yield strength of

the bulk material (σ_y) to its average grain size (D): $\sigma_y = \sigma_0 + \frac{K}{\sqrt{D}}$ where σ_0 is the friction stress and K is the macroscopic Hall-Petch coefficient (HPC), which represents the collective strengthening effect of all the grain boundaries in the polycrystal. One of the most common mechanisms that the Hall-Petch effect is attributed to is the strength needed for a dislocation pile-up to overcome the grain boundary (treated as an obstacle) to effect slip transmission. Extensive research into slip transmission phenomena in polycrystalline materials has unraveled its complexity via dependence on a multitude of local factors such as GB energy [18,19], atomic structure of GB [20], residual Burgers vectors [21–24], resolved shear stress on each slip system [24–26] and a combination of these factors [27–33] . While these are important to the eventual understanding of their effect on the HPC, an attempt to analyze the effect of crystallographic properties on the HPC forms an initial step to tackle this problem.

Many studies in the literature have reported that the HPC for face-centered cubic (FCC) and body-centered cubic (BCC) materi-

als are less sensitive to crystallographic texture [34–38] as compared to hexagonal close-packed (HCP) metals such as Mg and its alloys [10,39–41]. Texture variations can alter dominant deformation modes, on which the grain boundaries can have a different effect, which in turn can result in different values of the HPC [41]. Accordingly, various efforts have been made to estimate the HPC for a wide variety of alloys by considering the effect of texture, intergranular relationships, and a dependence of the slip system resistance on grain size [9,42–44]. To reflect these changes occurring at the microscale, the Hall-Petch relationship is specialized to the slip system level as $\tau^\alpha = \tau_0^\alpha + k_\mu^\alpha . L^{-1/2}$, where τ^α is the critical resolved shear stress of slip system α, τ_0^α is the critical resolved shear stress of slip system α of a theoretically infinite single crystal, k_μ^α the Hall-Petch coefficient of the slip system α (henceforth referred to as micro-Hall-Petch coefficient) and L is the slip system-level grain size [45–47]. Wang et al. [41] and Singh et al. [48] proposed an approach to estimate the k_μ^α using macroscopic tensile test data of Mg alloy samples with four different average grain sizes. They calculated the resolved shear stress of the dominant slip system at yielding by dividing the yield strength of the material by the average Schmid factor values of that specific slip system. The micro-Hall-Petch coefficient is then obtained from the slope of the linear regression model which assumes a linear relationship between the resolved shear stress data and the inverse square root of the average grain size. While their studies provide a rough estimate of k_μ^α, their approach does not consider the structure and geometry of the grain boundaries.

Several theoretical models have reported that the geometry and structure of the grain boundary (GB) plays an important role in impeding slip transmission within the material and hence contributing to the strength of polycrystalline materials [18,20,28]. However, experimental observations to accurately quantify the grain boundary strength and validate these theoretical models are primarily limited by the ability of experimental techniques to measure the stress field ahead of a slip band blocked by a grain boundary.

Recently, the development of high-resolution electron backscatter diffraction (HR-EBSD) technique provides the possibility of measuring the stress components locally in materials with the spatial resolution on the order of 100 nm [49]. Using this technique, the local stress concentration, ahead of dislocation pile-ups, has been successfully examined in commercial purity titanium [50–52], irradiated steel [53,54], and unalloyed Mg [55].

In this work, HR-EBSD measurements are analyzed using a continuum dislocation pile-up model to calculate the micro-Hall-Petch coefficient of the basal slip system for nine different grain boundaries in a deformed Mg-4Al sample. HR-EBSD is a surface measurement technique, while grain boundary descriptors such as GB tilt and twist angles are three-dimensional quantities not directly accessible through HR-EBSD. The novelty of this current work is the use of the focused ion beam (FIB) milling to obtain additional insights on the three-dimensional GB geometry for all nine grain boundaries. Based on the combined experimental data and model, different functional expressions are examined, which involve three-dimensional geometric descriptors of the respective GBs, and a functional form for the micro-Hall-Petch coefficient of the basal system depending on these descriptors is proposed. Their possible usage in crystal plasticity constitutive models is explored, and some outstanding issues are addressed.

2. Methods

2.1. Materials and experimental procedures

The alloy selected for this work was extruded Mg-4Al (wt.%) bar produced by CanmetMaterials. The as-extruded microstructure and texture of the material are shown in Fig. 1. The mi-

Table 1
List of GB misorientation angles and the corresponding rotation axis determined by EBSD of the selected GB-slip band interactions zones.

Grain Boundary ID	Misorientation (°)	Rotation Axis
1	73.70	$[\bar{4}\ 8\ \bar{4}\ \bar{3}]$
2	54.89	$[1\ 0\ \bar{1}\ 0]$
3	38.30	$[\bar{5}\ 1\ 4\ \bar{3}]$
4	39.21	$[5\ \bar{1}\ 4\ \bar{3}]$
5	26.65	$[\bar{7}\ 2\ 5\ 3]$
6	55.98	$[4\ \bar{5}\ 1\ 3]$
7	47.91	$[\bar{7}\ 2\ 5\ 0]$
8	89.01	$[\bar{7}\ 2\ 5\ 0]$
9	89.82	$[\bar{7}\ 2\ 5\ \bar{3}]$

crostructure contains equiaxed grains with an average grain diameter of 50 μm. Tensile test samples with the gage dimensions of 10 mm × 2 mm × 2 mm were cut using electrical discharge machining (EDM). Prior to mechanical testing, the samples were mechanically polished using standard metallographic techniques, with the final step using 0.05 μm polycrystalline diamond solution. The samples were then etched using an acetic-nitric solution (10 mL nitric acid, 5 mL acetic acid, 20 mL water, and 60 mL ethanol) for 3 s to reveal the GB structures under scanning electron microscopy (SEM).

The as-extruded microstructure and texture were measured using EBSD, as shown in Fig. 1a and Fig. 1b. The samples were then subjected to tensile loading parallel to the extrusion direction (shown in Fig. 1a) to produce slip bands. SEM imaging was then used to find and document the position of the blocked slip band-GB interactions. Two examples of such interactions are shown in Fig. 1c, and Fig. 1d, with slip bands, blocked at grain boundaries without evidence of slip transfer to the adjacent grain. Specific grain boundaries were chosen for this work based on the existence of blocked slip bands at GBs and various misorientation angles. Table 1 summarizes the GB misorientation and the corresponding rotation axis determined by EBSD of the selected GBs.

EBSD scans with the average size of 10 μm × 30 μm with a square grid and 200 nm step size, were captured near the slip band-GB interaction regions using FEI Quanta 650 ESEM equipped with an integrated Oxford AZtec EDS and EBSD system. The Kikuchi patterns were obtained at each step in the scan with a resolution of 1024 × 1024 pixels and saved in the TIFF image format with 12-bit depth.

CrossCourt4 (CC4) software package developed by BLG Vantage [56] was used for analyzing the Kikuchi patterns. For each Kikuchi pattern, 50 regions of interest (ROIs) with the 256 × 256 pixels in size were used. The ROIs were compared with the corresponding ROIs of the low-stress reference pattern of each grain using the cross-correlation method developed by Wilkinson et al. [49] to calculate the full stress tensor fields. The remapping algorithm developed by Britton and Wilkinson [57] was used during CC4 analysis to reduce the effect of minor lattice rotation on the assessment of stress tensor.

After the HR-EBSD measurement was completed, focused ion beam (FIB) milling was performed using a dual-beam FEI Helios Nanolab 650 microscope to lift out a lamella perpendicular to the GB line and the surface normal, to discover the GB tilt relative to the surface normal.

2.2. Numerical methods

While the blocked slip band in one grain is observed, it is also important to identify the most likely slip system to be activated in the adjacent grain where no slip bands are seen. The primary slip system in the adjacent grain that is likely to get activated is
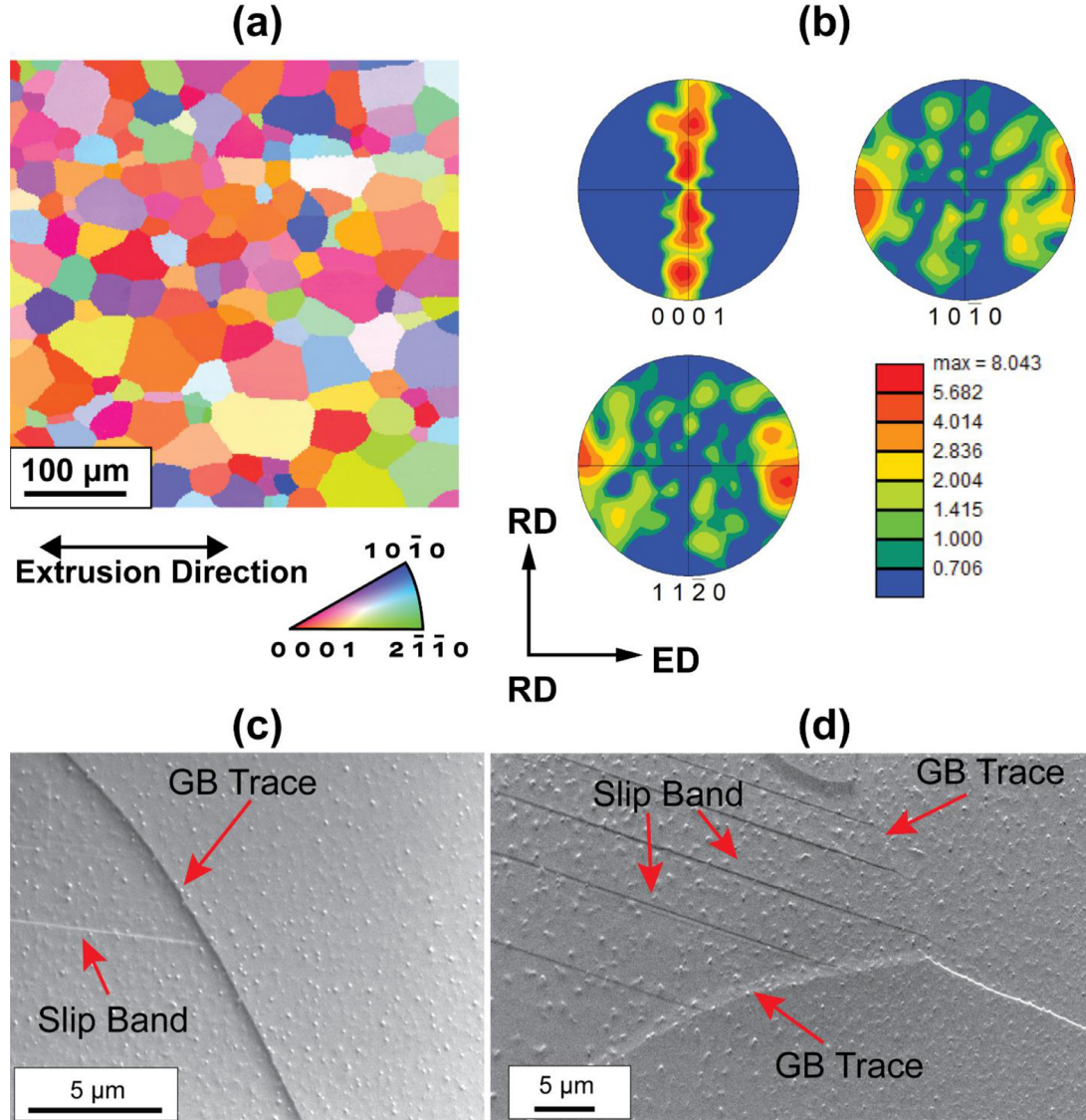
Fig. 1. (a) Representative microstructure and (b) pole figure of extruded Mg-4Al (wt.%) used in this study. The microstructure contains equiaxed grains with an average grain diameter of 50 μm. RD: Radial Direction; ED: Extrusion Direction (c),(d) Two examples of blocked slip bands at grain boundaries which blocked slip bands in one grain and no-slip transfer or slip band formation in the adjacent grain, is observed.

affected by factors such as slip orientation relative to loading and load redistribution due to the grain neighborhood. Crystal plasticity finite element (CPFE) simulations allow a detailed computational understanding of these factors. The single crystal constitutive model for CPFE was first calibrated by comparing the polycrystal stress-strain response with the experimental stress-strain curves. These parameters were then used to simulate the different GB neighborhoods to identify the likely primary slip system in the grains sharing the respective grain boundary of interest. All the crystal plasticity simulations were carried out using PRISMS-Plasticity [58,59], an open-source 3-D CPFE framework based on a fully implicit implementation of an elastoplastic single crystal model. Crystallographic slip, twinning, and re-orientation of crystals were assumed to be the primary mechanisms of plastic deformation. For a crystal with N slip/twin systems the slip resistance offered by slip system α at time t, $s^\alpha(t)$, depends on the plastic slip rates via the hardening law:

$$\dot{s}^\alpha(t) = \sum_{\beta=1}^{N} h^{\alpha\beta}\left|\dot{\gamma}^\beta\right|, \text{ where } s^\alpha(0) = s_0^\alpha \tag{1}$$

$$h^{\alpha\beta} = h_0^\beta\left(q + (1-q)\,\delta_{\alpha\beta}\right)\left(1 - \frac{s^\beta(t)}{s_{sat}^\beta}\right), \text{ (no sum on } \beta) \tag{2}$$

where the latent hardening is included through the coefficient q which is chosen to be 1, and $\delta_{\alpha\beta}$ denotes the Kronecker delta. s_0^α denotes the initial slip resistance of slip system α, while h_0^β and s_{sat}^β signify the hardening modulus and saturation stress, respectively, for slip system β. These three parameters were calibrated for each slip system such that the CPFE model predicts the experimental stress-strain response in the plastic regime satisfactorily. Additional details of the model, including elastoplastic decomposition, flow rule and constitutive update algorithm, are detailed in [60].

For the calibration step, the polycrystal idealized as an $8 \times 8 \times 8$ voxelated RVE was constructed, where each voxel was assigned a distinct orientation. Orientations were sampled from an EBSD map of a microstructure (Fig. 1a and Fig. 1b) with 856 grains to ensure that the texture was satisfactorily represented in the idealized polycrystal (Fig. 2a). This microstructure was subject to axisymmetric tension along the y direction up
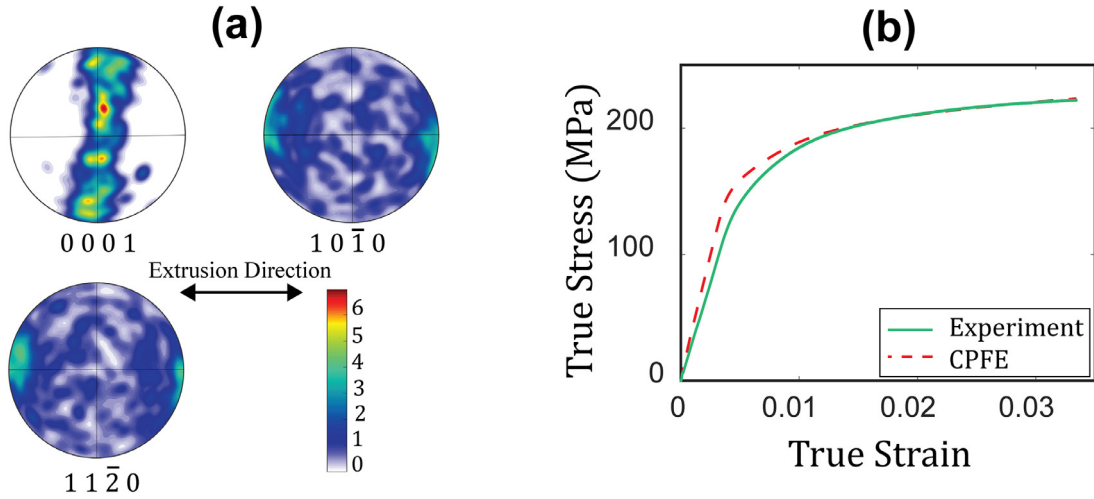
Fig. 2. (a) Pole figures of the polycrystalline RVE represented as an 8 × 8 × 8 voxelated grid with one orientation per voxel, (b) Comparison of simulated stress-strain response with experiment resulting in the calibrated parameters in Table 2.

Table 2
Initial slip resistance and hardening parameters post-calibration.

Mode	s_0^α	h_0^α	s_{sat}^α
Basal $<a>$	6.0	76.0	120.0
Prismatic $<a>$	78.0	163.0	150.0
Pyramidal $<a>$	78.0	163.0	150.0
Pyramidal $<c + a>$	140.0	187.0	150.0
Twin $<c + a>$	13.0	116.0	100.0

to approximately 3.5% strain. Fig. 2b depicts the comparison of stress-strain response from the simulation to the experiment at the end of calibration. The list of constitutive model parameters post-calibration is included in Table 2.

3. Results

3.1. Stress concentration calculation ahead of blocked slip bands at grain boundaries

Slip bands blocked at grain boundaries were identified using SEM (two examples of such regions are shown in Fig. 1c and Fig. 1d), and 10 μm × 30 μm regions around the interaction area were selected for HR-EBSD scans as shown in Fig. 3a. For each grain, a reference point for the measurement of stress was selected far away from the grain boundaries, where stress was assumed to be low relative to the GB vicinity. An example of a reference pattern site marked with a yellow cross is shown in Fig. 3a, and the corresponding high-quality image Kikuchi pattern is shown in Fig. 3b. For each Kikuchi pattern, 50 ROIs were used and compared with the corresponding ROIs of the reference pattern to calculate the distortion tensor and from that the full stress tensor (more details provided in Section 2.1). The stress components were obtained relative to the $x_1 x_2 x_3$ reference frame (Fig. 4a), which we refer to as the sample frame. An example of the full stress tensor as the output of HR-EBSD analysis is shown in Fig. 3c. The stress concentration induced by slip bands blocked at the GB can be clearly observed from the σ_{11}, σ_{12} and σ_{23} stress components. σ_{33} is negligible because the sample surface was unconstrained.

To calculate the shear stress resolved onto the slip system corresponding to the slip band, the slip system was first determined (explained in Section 3.2.2), and then the stress tensor was rotated to another axis system, $x_1^r x_2^r x_3^r$ as shown in Fig. 4a. In this axis system, x_1^r is the direction of the slip plane normal while x_3^r and x_2^r

are in the direction of the Burgers vector of the determined active slip system in the deformed grain (upper grain) and the direction perpendicular to it on the slip plane, respectively. Fig. 4b shows τ_{13}^r component of the rotated tensor, which represents the resolved shear stress of interest on the slip system corresponding to the slip band of the deformed grain.

In our previous work [55], the slip band blocked at the GB was interpreted as a pile-up of dislocations, which was then modeled using a 1D double-ended continuum dislocation pile-up. The theoretical model is briefly reviewed first.

In the 1D double-ended continuum dislocation pile-up model, the equilibrium dislocation distribution is obtained for the case when a spatially constant resolved shear stress is applied throughout a grain of size L. The balance between the applied stress and the dislocation-dislocation interactions results in an equilibrium dislocation distribution from which the stress field ahead of the pile-up [61] is obtained as

$$\tau_p(X) = \tau \; . \left[\frac{X + \frac{L}{2}}{\sqrt{\left(X + \frac{L}{2}\right)^2 - \left(\frac{L}{2}\right)^2}} - 1 \right] \tag{3}$$

where $\tau_p(X)$ represents the resolved shear stress ahead of the pile-up, L is the grain size, and X is the coordinate measured from the grain boundary. Considering a specific slip system of interest indexed as α, substituting the phenomenological micro-Hall-Petch equation [34,45], $\tau = \tau^\alpha = \tau_0^\alpha + \frac{k_\mu^\alpha}{\sqrt{L}}$ into Eq. (4) yields

$$\tau_p(X) = \left(\tau_0^\alpha + \frac{k_\mu^\alpha}{\sqrt{L}} \right) \left[\frac{X + \frac{L}{2}}{\sqrt{\left(X + \frac{L}{2}\right)^2 - \left(\frac{L}{2}\right)^2}} - 1 \right] \tag{4}$$

where τ_0^α is the critical resolved shear stress of slip system α of a theoretically infinite single crystal, k_μ^α the micro-Hall-Petch coefficient of the slip system α, L is the slip system-level grain size, and X is the distance from the GB, as denoted in Fig. 4b. The micro-Hall-Petch coefficients were computed for different GB types by fitting the experimentally measured stress field ahead of the pile-up (Fig. 4b) to the calculation (Eq. (4)). It must be noted that using a 1D continuum dislocation pile-up model is an oversimplification of the actual physics, which is much more complicated. Additionally, the back-stress that might arise from GND distributions in the vicinity of the GB is not considered explicitly in the pile-up model. Their importance has been demonstrated in the context
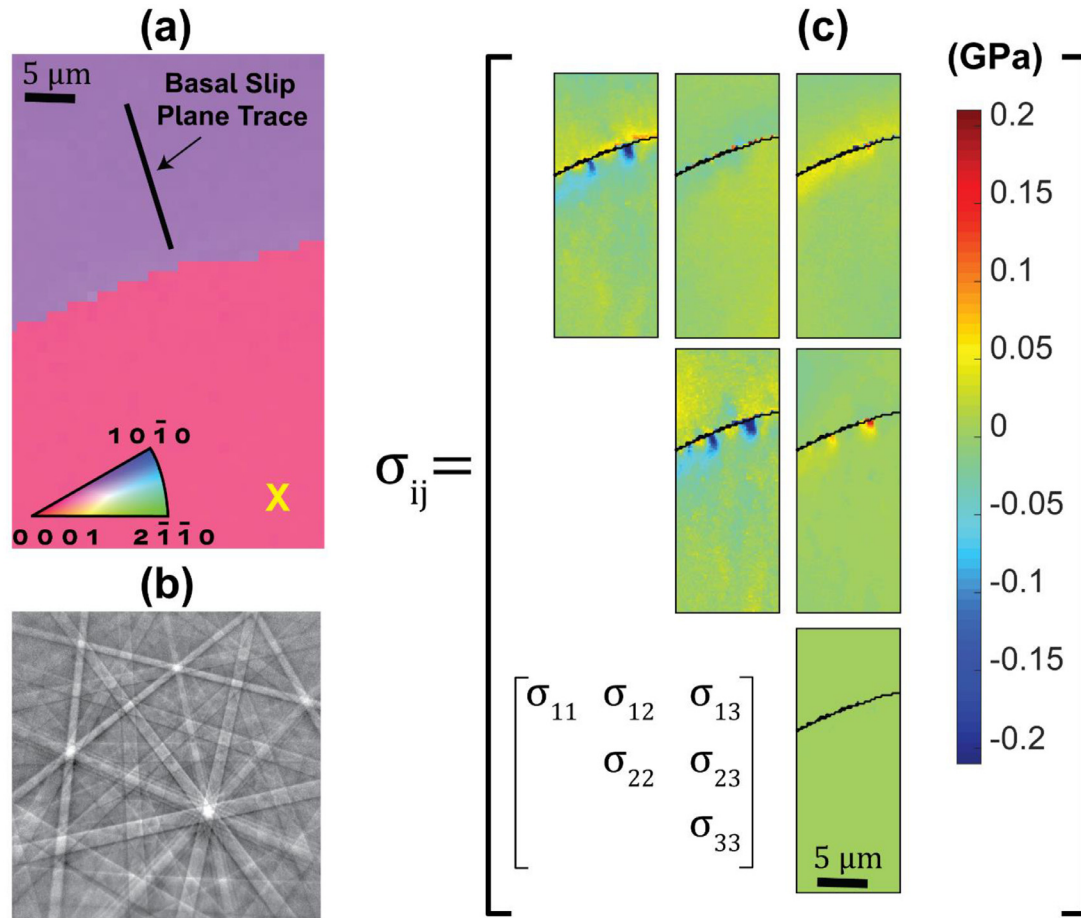
Fig. 3. (a) An example of selected 10 μm × 30 μm regions around the slip band-GB interaction for HR-EBSD scans. (b) Kikuchi diffraction pattern of the reference point marked by a yellow cross in Fig. 3a. (c) An example of HR-EBSD output which is a full stress tensor calculated in the sample frame. (For interpretation of the references to colour in this figure legend, the reader is referred to the web version of this article.)

Table 3
Micro-Hall-Petch coefficient of the basal slip system for different grain boundaries.

Grain boundary ID	1	2	3	4	5	6	7	8	9
Slip System Level Grain Size (μm)	48	55	27	8	65	21	50	60	48
k_μ^{basal} (MPa.m$^{1/2}$)	0.164 ± 0.02	0.091 ± 0.01	0.149 ± 0.02	0.172 ± 0.02	0.054 ± 0.01	0.108 ± 0.01	0.070 ± 0.01	0.143 ± 0.01	0.184 ± 0.02

of large grained titanium [62] where correlations were drawn between GND content and geometric metrics of the GB. However, quantification of this back-stress for informing micromechanical models like the present pile-up model is yet to be performed. In the interest of drawing a simple analogy to a blocked slip band and obtaining first-order analytical expressions, we have resorted to the aforementioned model 1D continuum pile-up model without GND induced back-stress.

A line scan was taken along the slip direction of the deformed grain (upper grain) but continued to the lower grain, labeled by X direction in Fig. 4b, to capture the stress profile ahead of the slip band pile up at the GB as shown in Fig. 4c. This stress was then resolved onto the active slip system to yield the resolved shear stress profile ahead of the blocked slip band, which was fitted with Eq. (3). The experimental data follow a similar trend as the dislocation pile-up model presented in Eq. (3) (Fig. 4c). The micro-Hall-Petch coefficient of the active slip system α, can be obtained by curve fitting the experimental stress profile with the continuum dislocation pile-up model. k_μ^α for all analyzed grain boundaries are measured and reported in Table 3. Since the active slip systems

of the deformed grains in all different boundaries studied in this work were basal slip systems (Table 6), τ_0^α is computed by incorporating the effect of solid solution strengthening due to 4 wt.% Al [63] resulting in $\tau_0^\alpha = 4.34$ MPa. Accordingly, the calculated micro-Hall-Petch coefficient is denoted as k_μ^{basal}.

3.2. Understanding the effect of grain boundary on the micro-Hall-Petch coefficient

The goal of this study is first to calculate the micro-Hall-Petch coefficient of various type of grain boundaries (Section 3.1) and then correlate k_μ^α values with the quantitative geometrical expressions describing the slip band-GBs interactions. Fig. 5 shows a schematic of slip transfer across a grain boundary. θ is the angle between the two slip plane traces on the GB plane, κ is the angle between slip directions (Burgers vector), ψ is the angle between slip plane normal directions, and δ is the angle between the incoming slip direction and the intersection of the incoming slip plane with the GB plane. $\vec{b}$, $\vec{n}$, $\vec{l}$, and $\vec{d}$ represent the Burgers vector of the slip plane, the slip plane normal, the intersection line of
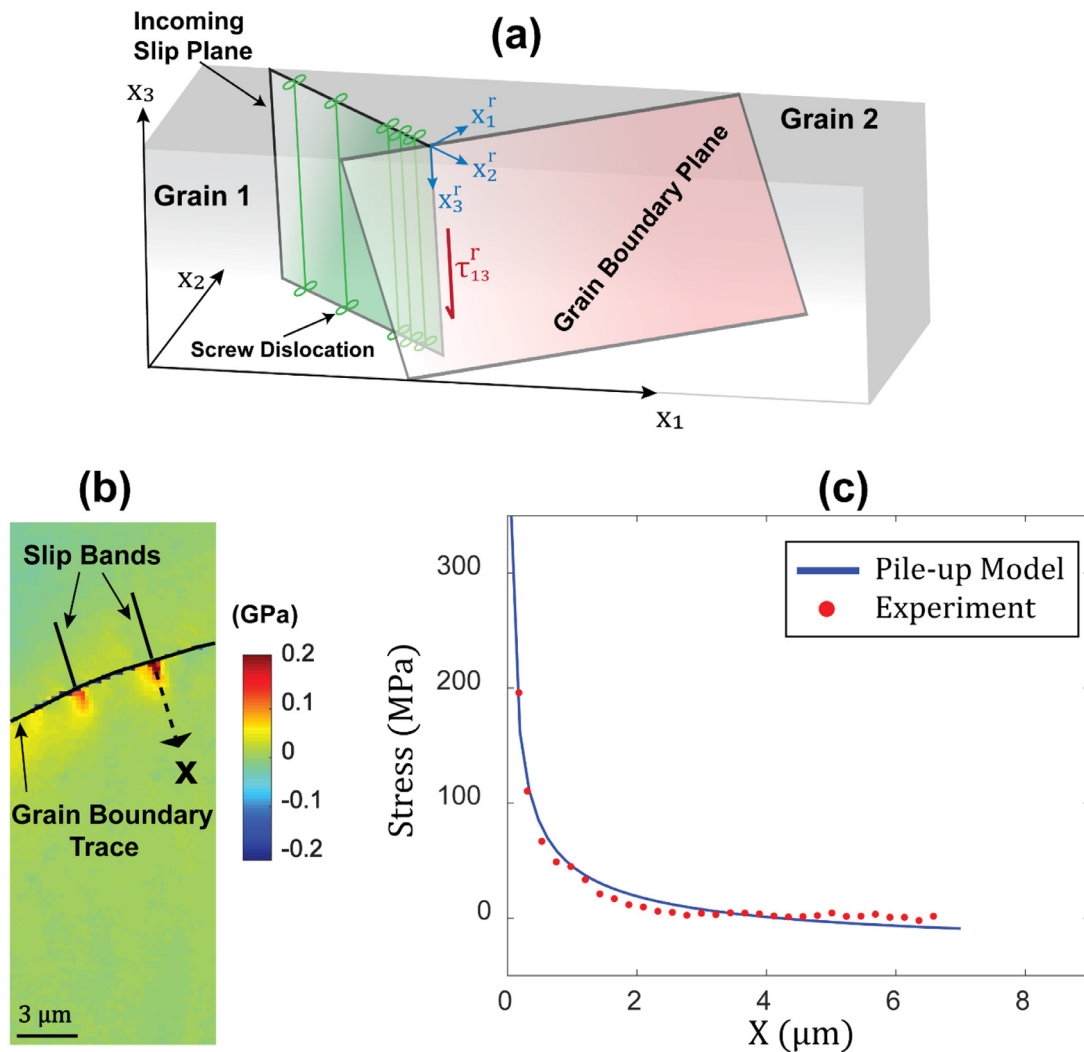
Fig. 4. (a) Schematic of a slip band as a dislocation pile-up at a GB. HR-EBSD is used to measure the stress in the sample frame $x_1x_2x_3$. To calculate the shear stress resolved onto the active slip system observed experimentally by the slip band (τ_{13}^r), the stress tensor was rotated into another axis system, $x_1^r x_2^r x_3^r$. (b) HR-EBSD map of resolved shear stress τ_{13}^r onto the active slip system in the upper grain. The stress concentration ahead of pile up at GB can be observed. The solid lines represent the position of the slip bands, and the dashed line with an arrowhead indicates the direction along which the stress profile shown in Fig. 4c was extracted. (c) The resolved shear stress profile ahead of a slip band blocked by a GB with comparison to the continuum dislocation pile-up model to calculate the micro-Hall-Petch coefficient of each individual GB.

slip plane and GB plane, and the slip direction, respectively. To find the above mentioned quantitative geometrical expressions for each slip band-GB interaction cases studied in this work, it is required to find the grain boundary plane orientation, the slip systems associated with the observed slip band at the grain boundary and the outgoing slip system of least resistance. The outgoing slip system of least resistance is interpreted as the slip system in the adjacent grain (Grain 2 in Fig. 4), which offers the least resistance to transmission of the slip system in Grain 1. Crystal plasticity simulations are set up for the grain boundary neighborhoods to provide exactly this piece of information, the details of which are described later.

3.2.1. Grain boundary plane orientations

The grain boundary plane (Fig. 6a) can be described by the grain boundary *trace* angle (α), the angle between the line made by grain boundary plane on the sample surface and the loading axis (extrusion direction) (Fig. 6b), and the grain boundary *plane* angle (β), the angle between the grain boundary plane and the sample surface normal (Fig. 6c). The grain boundaries were first examined using SEM, and the plan view images of the grain boundaries were obtained after the horizontal direction was

aligned with the loading axis, as shown in Fig. 6d. This image was then post-processed manually to compute α. Subsequently, focused ion beam (FIB) milling on a FEI Helios Nanolab 650 was used to prepare cross-section lamellae of grain boundaries, as shown in Fig. 6e. This image was then post-processed manually to obtain β. Since the slip band was not visible in the cross-sectional images, care was taken to ensure that these cross-sections were close enough to the slip band-GB intersection region to minimize error in the measured β value.

3.2.2. Grain neighborhood simulations

CPFE simulations were performed on microstructural neighborhoods of each GB of interest, consisting of the grains sharing that boundary and a few other surrounding grains. The aim was to find the active slip system associated with the observed slip band and predict the outgoing slip system of the least resistance. Since EBSD maps were available for just one section (sample surface), three-dimensionality of the problem was preserved by extruding the 2D section to obtain a one element slice of unit thickness, also implying that the subsurface grains were not considered as a part of the simulation. This is not problematic since the surface of the
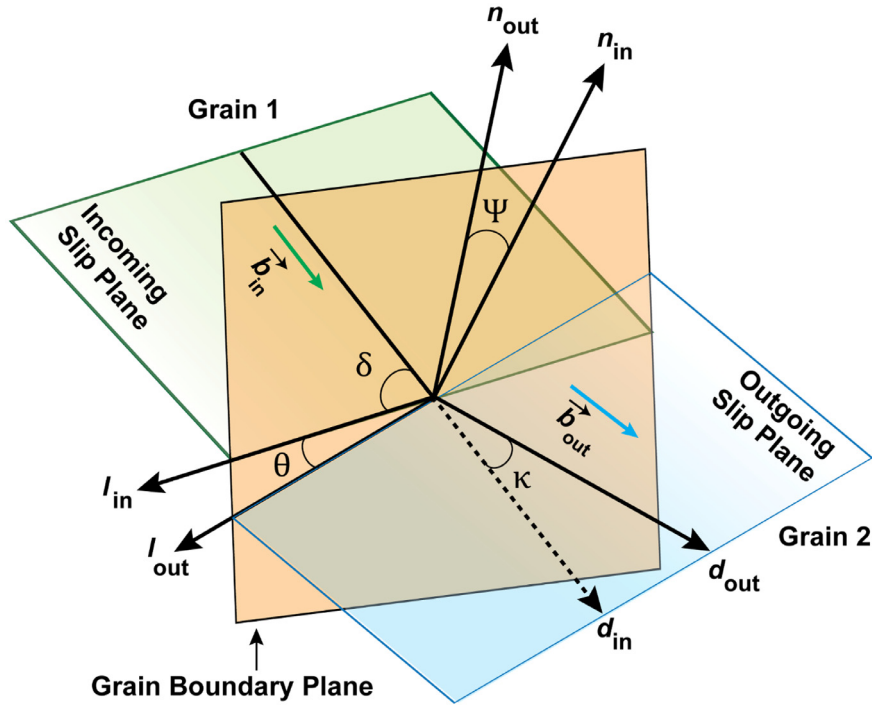
Fig. 5. Schematic of a slip transmission through a grain boundary.

Table 4
Grain boundary plane orientation for different grain boundaries studied in this work.

GB ID	1	2	3	4	5	6	7	8	9
α (°)	58.35	104.59	40.21	109.96	91.98	17.75	91.33	65.47	16.43
β (°)	76.28	0.51	24.81	49.66	11.79	67.78	13.30	45.06	66.82

simulated microstructure is a traction-free surface in the experimental test as well. Earlier work [64] showed that under such circumstances, the inclusion of subsurface grains in the simulation affected the basal slip activity to a minor extent relative to simulations on the microstructure slice. Additionally, to overcome the lack of knowledge of the state of stress or displacements at the boundary of those neighborhoods, boundary conditions were enforced as follows:

(i) The x and y components of displacements were enforced on the lateral boundaries based on a constant velocity gradient reminiscent of uniaxial tension along direction.

$$L = \dot{F}F^{-1}, \ F(0) = I \ \Rightarrow \ F = \exp(tL); \ L = \begin{bmatrix} -0.5 & 0 & 0 \\ 0 & 1 & 0 \\ 0 & 0 & -0.5 \end{bmatrix} \quad (5)$$

$$u_x = F_{11}x + F_{12}y + F_{13}z, \ u_y = F_{21}x + F_{22}y + F_{23}z \quad (6)$$

where L is the velocity gradient, F is the deformation gradient, t is the time, and u_x and u_y are the x and y components of the displacement, respectively.
(ii) The $x - y$ face at $z = 0$ is constrained from displacing along the z direction while the opposite face is treated as a free surface.

Slices of the simulated microstructure were deformed to a strain of approximately 2% where the grains of interest show some slip activity in order to identify the most active system, which is computed as follows. For each element of the FE mesh, the accumulated slip for each slip system was computed based on the information available at the integration points. The most active slip systems were then identified as the one with the highest accumulated slip at the end of deformation. These IDs refer to those appearing in column 2 of Table 4.

The neighborhood microstructure corresponding to Grain Boundary 1 is shown in Fig. 7a which consists of 21 grains. Fig. 7b shows a map of the most active slip systems for each voxel of the entire microstructure visualized by their ID. It is evident that in the grain neighborhood shown in Figs. 7a and 7b, basal slip is predicted to be the most active slip system. Grain Boundary 1 and the grains of interest are depicted in Fig. 7c identifying the grain containing the slip band and the grain blocking the slip band, Fig. 7d shows a map of the most active slip systems for all voxels belonging to the two grains of interest and Fig. 7e depicts the von Mises equivalent stress map for the simulated microstructure. For the grain containing the slip band, CPFE augments the slip trace analysis because slip traces only convey information about the slip plane, but nothing is known about the slip direction. That is where the CPFE simulation results dictate the choice of the most active slip system, which is correlated with the slip trace in that grain. For the grain blocking the slip band (the adjacent grain) the most active slip system (potentially outgoing slip system) is interpreted as the one offering the least resistance to the slip band so that when slip transmission ensues, it occurs with the highest probability on this most active slip system. For this purpose, the region at the grain boundary containing the slip band in the real microstructure was identified by its corresponding voxel (V1) in the voxelated structure. Then the voxel next to V1 in the adjacent grain was identified, and the most active slip system was obtained. This slip system was chosen as the one offering the least resistance
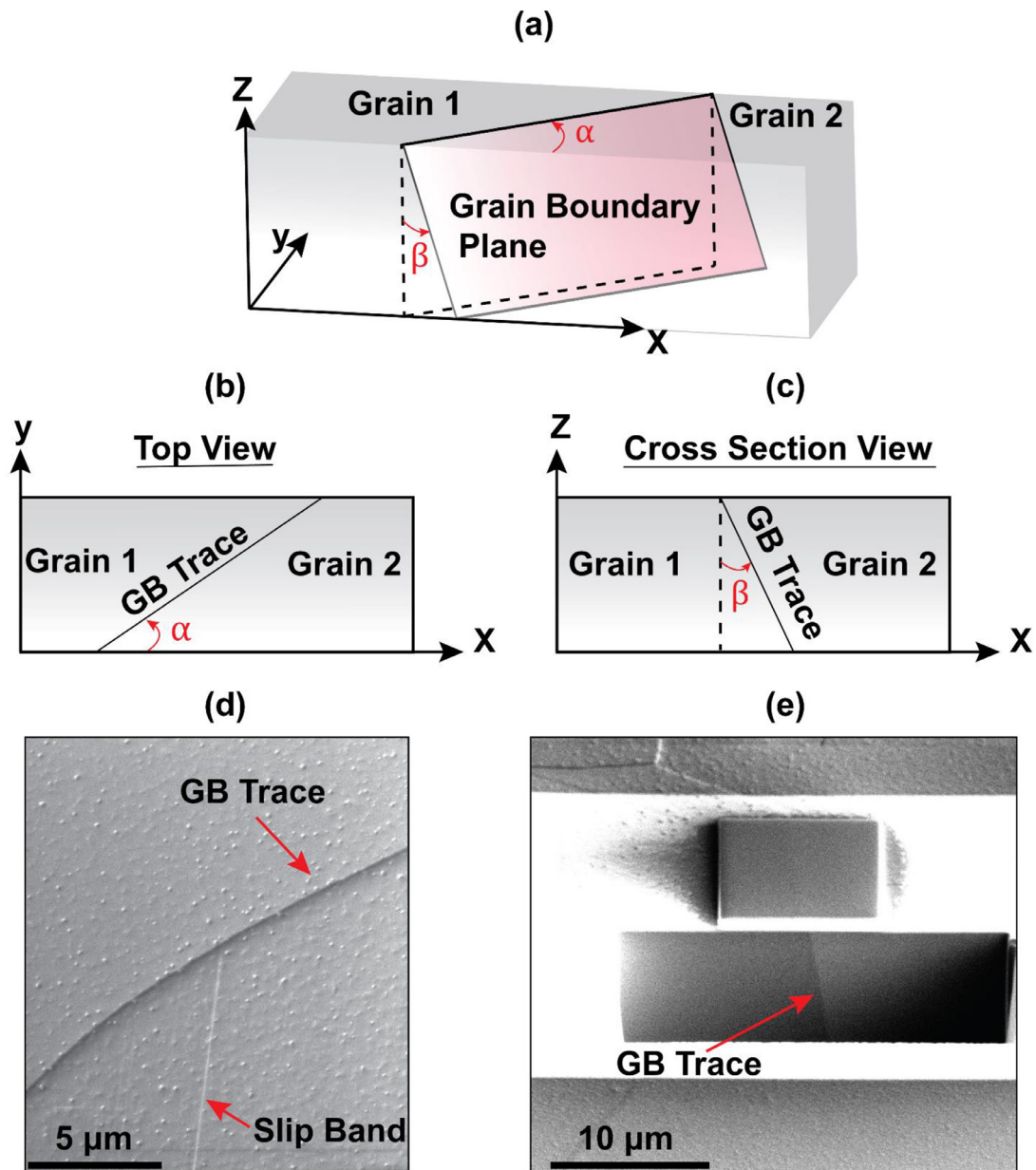
Fig. 6. (a) Schematic showing the grain boundary plane, which can be described by (b) the grain boundary trace angle, and (c) the grain boundary plane angle. (d) The grain boundary trace angle (α) can be measured using the plan view image of the grain boundary. (e) The grain boundary plane angle (β) can be measured using cross-section lamellas of grain boundary prepared by FIB milling. (For interpretation of the references to colour in this figure legend, the reader is referred to the web version of this article.)

to the slip band. For Grain Boundary 1 based on prior arguments, the most active slip system in the adjacent grain has ID 1 which corresponds to the system (0001)[11$\bar{2}$0] while the slip system corresponding to the slip bands has ID 3 which corresponds to the system (0001)[1$\bar{2}$10].

3.3. Relationship between the micro-Hall-Petch coefficient and the quantitative geometrical expressions describing the slip band-GB interactions

Table 5 summarizes the slip systems of the identified incoming and potentially outgoing (offering the least resistance) slip system for each GB analyzed. The quantitative geometrical expressions (θ, κ, ψ, δ) were calculated for each GB cases, are also listed in Table 5. The total number of grains for each of the

simulated microstructures described in Section 3.2 is included in Table 5.

The micro-Hall-Petch coefficient values presented in Table 3 plotted against the angle between the two slip plane traces on the GB plane (θ) (Fig. 8a), the angle between slip directions (κ) (Fig. 8b), the angle between slip plane normal directions (ψ) (Fig. 8c), and the angle between the incoming slip direction and the intersection of the incoming slip plane with the GB plane (δ) (Fig. 8d). In order to quantify the correlation between the micro-Hall-Petch coefficient values and each of the quantitative geometrical expressions (θ, κ, ψ, δ), the R-squared value, also known as the coefficient of determination, was computed. This statistical correlation parameter is an indicator that ranges in value from 0 to 1. The higher the R-squared value, the more reliable the linear regression is. The calculated R-squared values are shown in each plot.

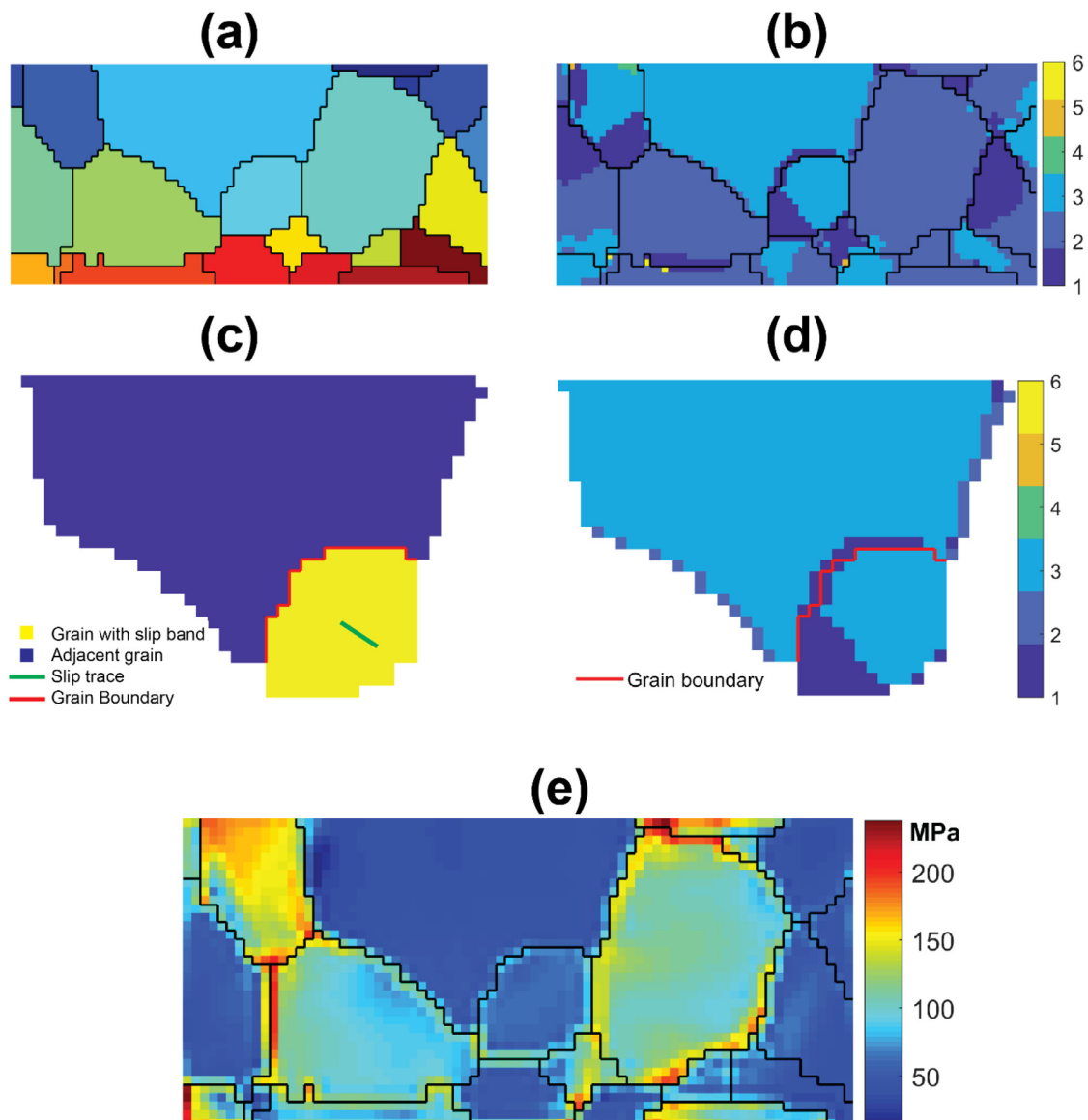**Fig. 7.** (a) Neighborhood microstructure related to Grain Boundary#1, and (b) its corresponding map of most active slip system ID (c) Microstructure of the grains sharing the grain boundary of interest, identifying the grain containing the slip band, the grain blocking the slip band, the grain boundary and the trace of the basal plane, and (d) a map of the most active slip systems in each voxel belonging to the grains sharing the grain boundary. Legend numbers (1–6) refer to the active slip system IDs in Table 4, and (e) von Mises equivalent stress map of the simulated microstructure.

4. Discussion

The blocked slip bands at the grain boundaries in Mg-4Al were investigated using HR-EBSD, cross-correlation analysis, and CPFE. Nine different grain boundaries were selected based on the existence of blocked slip bands at the GBs and various misorientation angles (Table 1). CPFE and trace analysis (Section 3.2.2) confirmed that the slip band in each case was associated with a basal slip system (Table 5). The full stress concentration tensor induced by the slip bands blocked at the GB was calculated using the HR-EBSD technique combined with the cross-correlation analysis (Section 3.1). The stress field was then resolved onto the active slip plane of the incoming slip band, and the resulting resolved shear stress profile was fit with the continuum dislocation pile-up model at a GB (Eq. (3)) to obtain the micro-Hall-Petch coefficient of each GB case (Table 3). The k_μ^{basal} values vary from 0.054 MPa $-$ m$^{1/2}$ to

0.184 MPa $-$ m$^{1/2}$ suggesting that the stress concentration ahead of a pile-up depends on the strength of each individual GB against slip transmission.

The k_μ^{basal} values are plotted against the quantitative geometrical expressions ($\theta, \kappa, \psi, \delta$), which describe the slip band-GBs interactions, as shown in Fig. 8. The R^2 value used to find out which angle has a major effect on k_μ^{basal}. R^2 is higher for Fig. 8a, which depicts the plot of k_μ^{basal} against the angle between the two slip plane traces on the GB plane (θ), suggesting the critical role of the grain boundary plane orientations in stress concentration ahead of pile up. The angle between slip plane traces on the GB plane also appears in Davis [65], where the investigations into slip continuity (transmission) motivated the stepped dislocation (see Fig. 9) formation energy as a determining factor for slip transmission. The work done in order to overcome the energy barrier for stepped dislocation formation, under a number of assumptions of the the-
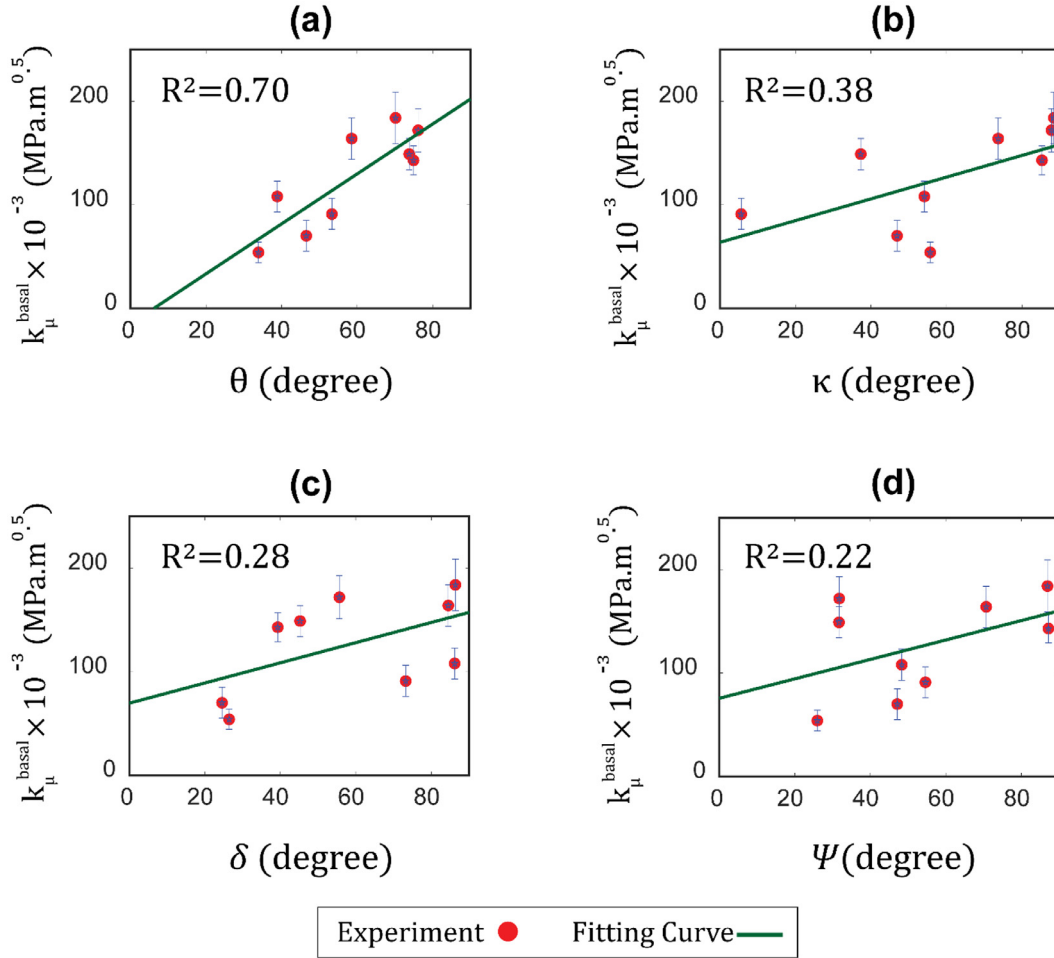
Fig. 8. The micro-Hall-Petch coefficient values against (a) the angle between the two slip plane traces on the GB plane (θ). (b) the angle between slip directions (κ). (c) the angle between slip plane normal directions (ψ). (d) the angle between the incoming slip direction and the intersection of the incoming slip plane with the GB plane (δ).

Table 5
Slip and twin systems for Mg alloys.

Slip System	ID	Slip Direction	Slip Plane
Basal	1	$[11\bar{2}0]$	(0001)
	2	$[\bar{2}110]$	(0001)
	3	$[1\bar{2}10]$	(0001)
Prismatic$<a>$	4	$[1\bar{2}10]$	$(10\bar{1}0)$
	5	$[2\bar{1}\bar{1}0]$	$(01\bar{1}0)$
	6	$[11\bar{2}0]$	$(\bar{1}100)$
Pyramidal$<a>$	7	$[1\bar{2}10]$	$(10\bar{1}1)$
	8	$[\bar{2}110]$	$(01\bar{1}1)$
	9	$[\bar{1}\bar{1}20]$	$(\bar{1}101)$
	10	$[\bar{1}2\bar{1}0]$	$(\bar{1}011)$
	11	$[2\bar{1}\bar{1}0]$	$(0\bar{1}11)$
	12	$[11\bar{2}0]$	$(1\bar{1}01)$
Pyramidal$<c + a>$	13	$[\bar{1}\bar{1}23]$	$(11\bar{2}2)$
	14	$[1\bar{2}13]$	$(\bar{1}2\bar{1}2)$
	15	$[2\bar{1}\bar{1}3]$	$(\bar{2}112)$
	16	$[11\bar{2}3]$	$(\bar{1}\bar{1}22)$
	17	$[\bar{1}2\bar{1}3]$	$(1\bar{2}12)$
	18	$[\bar{2}113]$	$(2\bar{1}\bar{1}2)$
Twin$<c + a>$	19	$[\bar{1}011]$	$(10\bar{1}2)$
	20	$[10\bar{1}1]$	$(\bar{1}012)$
	21	$[\bar{1}101]$	$(1\bar{1}02)$
	22	$[1\bar{1}01]$	$(\bar{1}102)$
	23	$[0\bar{1}11]$	$(01\bar{1}2)$
	24	$[01\bar{1}1]$	$(0\bar{1}12)$

oretical model, was shown to be proportional to $\sin(\theta)$, hence motivating the consideration of θ as an important parameter in determining the strength of the GB to slip transmission and consequently the micro-Hall-Petch coefficient.

The angle between slip directions (κ) (Fig. 8b) is the second most effective (R^2=0.38) quantitative geometrical expression in determining the k_μ^{basal}. Previous studies [66,67] have reported that if the slip planes in two neighboring grains possess the same grain boundary trace and the Burgers vectors of dislocations are parallel (κ=0), then the dislocations in one grain can pass unhindered through the grain boundary into the adjacent grain. Consequently, increasing κ could result in an increase in the stress concentration ahead of pile up. It worth noting that since the incoming slip systems and predicted outgoing slip systems for all the nine-grain boundaries studied in this work are basal slip systems, the magnitude of residual Burgers vector (RBV) is directly proportional to $\sin(\frac{\kappa}{2})$ which clearly increases with κ. The RBV has been previously studied as a criterion to evaluate the strength of a GB against slip transmission [68–71].

As shown in Fig. 8c and 8d, k_μ^{basal} does not show a noticeable correlation with the ψ, the angle between slip plane normal directions, and δ, the angle between the incoming slip direction and the intersection of the incoming slip plane with the GB plane. This is because ψ does not capture the grain boundary plane orientations, which is present in the definition of θ, while δ does not have any information about the neighboring grain.

Taking into account both the geometrical and energetics aspects of k_μ^α, the following relationship is proposed:

$$k_\mu^{basal} = K^{basal}(1 - \cos(\theta)\cos(\kappa))^c; c > 0 \qquad (7)$$

where K^{basal} and c are model parameters. The factor $\cos(\theta)\cos(\kappa)$ was initial proposed by Lee–Robertson–Birnbaum [61,72,73] as be-

Table 6
Summary of the list of the incoming slip system and the predicted potentially outgoing slip system of each GB, and the quantitative geometrical expressions ($\theta, \kappa, \psi, \delta$) describing the slip band-GB interactions associated with each GB.

| GB ID	Number of grains in the simulated microstructure	Incoming Slip System	Outgoing Slip System	θ (°)	κ (°)	ψ (°)	δ (°)
1	21	$(0001)[1\bar{2}10]$	$(0001)[11\bar{2}0]$	58.54	73.75	70.68	84.55
2	21	$(0001)[1\bar{2}10]$	$(0001)[1\bar{2}10]$	53.31	5.61	54.59	73.21
3	24	$(0001)[\bar{2}110]$	$(0001)[\bar{2}110]$	73.79	37.30	31.70	45.24
4	34	$(0001)[11\bar{2}0]$	$(0001)[11\bar{2}0]$	76.16	87.81	31.77	55.64
5	17	$(0001)[\bar{2}110]$	$(0001)[1\bar{2}10]$	33.87	55.69	25.95	26.46
6	28	$(0001)[1\bar{2}10]$	$(0001)[1\bar{2}10]$	38.84	54.14	48.32	86.18
7	16	$(0001)[\bar{2}110]$	$(0001)[\bar{2}110]$	46.52	46.94	47.13	24.57
8	21	$(0001)[1\bar{2}10]$	$(0001)[1\bar{2}10]$	74.92	66.16	87.18	34.41
9	25	$(0001)[11\bar{2}0]$	$(0001)[\bar{2}110]$	70.16	88.42	86.91	86.38
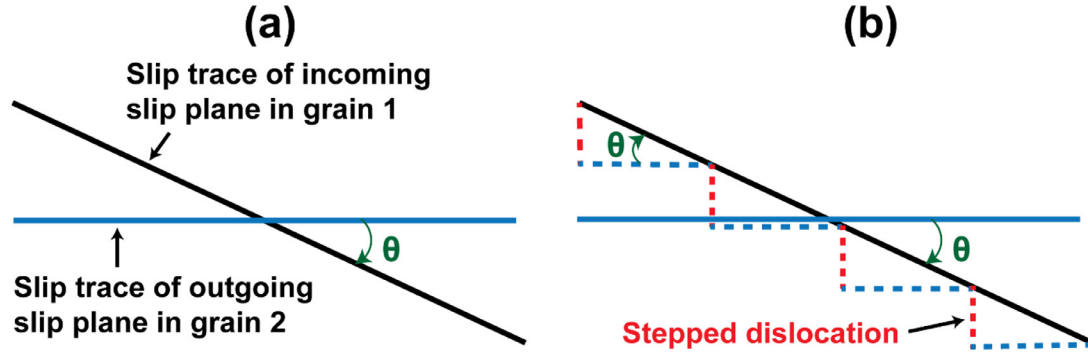
Fig. 9. (a) Schematic of slip traces of incoming and outgoing slip planes looking into the grain boundary plane. (b) Schematic of the formation of a stepped dislocation in grain 2 when a dislocation crosses from grain 1. The dotted line represents the dislocation in grain 2. [65].
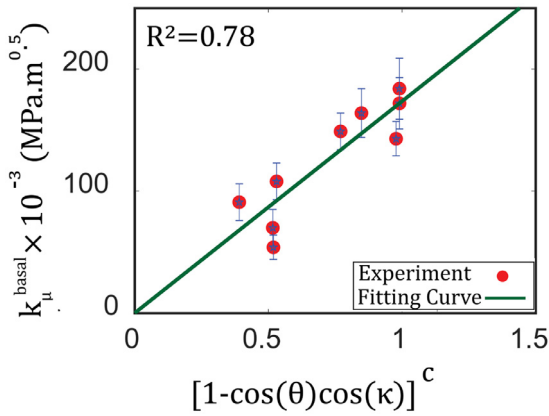

Fig. 10. The basal slip system micro-Hall-Petch coefficients (k_μ^{basal}) for the nine-cases are plotted against the factor $(1 - \cos(\theta)\cos(\kappa))^c$ where the model parameters K^{basal} and c were obtained from fitting the data points to a power-law. For this fit, R^2 is 0.78 which reflects close to the linear relationship between k_μ^{basal} and $(1 - \cos(\theta)\cos(\kappa))^c$.

ing relevant in the context of determining the outgoing slip system as a result of slip transmission across grain boundaries, based on in situ straining TEM experiments on FCC alloys. This relationship agrees with the Lim et al. [74] study where the strengthening effect of grain boundaries in Fe–3%Si was modeled by defining the grain boundary obstacle stress τ_{obs} as $\tau_{obs} = (1 - \cos(\theta)\cos(\kappa)) \, \tau^*$ where τ^* represents the maximum obstacle strength. The Hall-Petch coefficient is known to be correlated with the GB obstacle stress [75] and hence is indirectly related to the factor $(1 - \cos(\theta)\cos(\kappa))$.

k_μ^{basal} values obtained for the nine different cases in this study (Table 2) were fit with Eq. (7) obtaining the model parameters

$K^{basal} = 0.173 \pm 0.083$ MPa $- \text{m}^{1/2}$ and $c = 1.04$. For the nine cases, k_μ^{basal} values are plotted against $(1 - \cos(\theta)\cos(\kappa))^c$ as shown in Fig. 10. R^2 value of 0.78 indicates the good correlation between the k_μ^{basal} and the proposed relationship. The aforementioned approach and findings are similar in spirit to the suggestions made by Guo [76] where a full three-dimensional analysis of the grain boundary geometry was deemed necessary to obtain a well-informed relationship between the stress concentration induced by blocked slip band at a grain boundary.

One may notice that the obtained values for k_μ^{basal} or K^{basal} may not be in complete agreement with the macroscopic Hall-Petch coefficients reported in the literature for Mg-4Al. For example, Deda et al. [77] obtained the value of 0.31 MPa $- \text{m}^{1/2}$ for the macroscopic Hall-Petch slope of Mg-4Al. This discrepancy highlights the need for understanding the relationship between the macroscopic Hall-Petch coefficients and the strength of each grain boundary identified by micro-Hall-Petch coefficients. Although there are few studies on this topic [41,44], what is still missing is a procedure to estimate the macroscopic Hall-Petch slope considering the effect of multiple factors simultaneously like texture, loading direction, alloying, misorientation distribution, etc. Eq. (7) addresses part of this issue by encoding the effect of geometrical relationships into parameters quantifying size-effect at the slip system level. This must necessarily be complemented by some homogenization scheme to obtain estimates of the macroscopic Hall-Petch slope, which will be a subject of future work.

Crystal plasticity simulations have proven to be an indispensable tool in guiding our understanding of the effect of microstructure on the elastoplastic material behavior of polycrystalline solids. While classical crystal plasticity constitutive formulations provide a sound theoretical basis for modeling, their ability to incorporate microstructural size effect informed by experiments has been quite

limited. The experiments performed in this work combined with adequate post-processing of the data can augment crystal plasticity models, where the micro-Hall-Petch equation can be used to modify the slip resistance based on the micro-Hall-Petch coefficient and some measure of the grain size. More importantly, since the current work proposes a functional form for the micro-Hall-Petch coefficient depending on the geometric properties of a grain and its immediate neighbors, the effect of texture can be directly encoded into this coefficient. Furthermore, instead of resorting to the average grain size for the entire microstructure, each point in a grain can be assigned an effective distance from the grain boundary, which can be used as the measure of grain size for that point. Once crystal plasticity models are appropriately calibrated, they can also be used to generate macroscopic Hall-Petch slope datasets amenable to data-mining approaches [78], which can furnish a pipeline (as opposed to a simple formula) to estimate the macroscopic Hall-Petch slope for a complex microstructure.

It is important to note that while the functional dependence of the micro-Hall-Petch coefficient is useful, crystal plasticity simulations may not predict macroscopic stress-strain curves consistent with experiments if these values are directly used to modify the slip resistances. This discrepancy can be attributed to multiple factors. Firstly, the analysis described in this work relies on data obtained from the vicinity of a slip band blocked by a grain boundary, which is a local measurement. Crystal plasticity simulations, however, are unable to model a slip band since they capture the physics in an average sense, i.e., the slip band itself is not modeled, but the accumulated slip in a grain conveys something about the accommodation of plastic deformation and the possibility of slip bands. Hence the attempt to use the micro-Hall-Petch coefficient from such local experiments into crystal plasticity simulations must be accompanied by a sensible scaling of the coefficient. Secondly, estimates of the micro-Hall-Petch coefficient have been obtained when a sufficient number of blocked slip bands were visually identified, and this meant deforming the sample to a higher strain than where the onset of plasticity actually occurs. Along with blocked slip bands, there were also grain boundaries through which slip transmission occurred, which were not the subject of this study but which clearly contribute to the polycrystalline size effect. It is still unclear how the information from transmitted slip and blocked slip bands can be used together to better estimate the micro-Hall-Petch coefficient that can be directly embedded into crystal plasticity constitutive models to predict the macroscopic stress-strain curves and Hall-Petch effect correctly. Finally, the stress profile ahead of a blocked slip band is expected to change depending on the accumulated plastic strain, and hence the total strain to which the sample was deformed. In other words, if the sample was deformed to a higher value of strain and the slip bands identified earlier continued to be blocked, a higher value of the micro-Hall-Petch coefficient would be expected to fit the resolved stress measurements. This begs the question as to which value would be appropriate. One way to bypass the previous issues is to consider only the dependence of the micro-Hall-Petch coefficient on the geometric parameters while selecting K^{basal} by calibrating stress-strain curve predictions from CPFEM to experiments. This also demands an acceptable representation of the grain boundary in the discretization of the microstructure because the $[\cos(\theta)\cos(\kappa)]$ factor depends on the grain boundary plane orientations and hence is sensitive to the discretization as well. All these issues represent challenges to incorporating the results from this work into crystal plasticity constitutive models and setting up acceptable simulations. This will be a subject of future work.

5. Conclusions

- High resolution electron backscatter diffraction method was used to measure the local stress ahead of blocked slip bands at grain boundaries in a deformed Mg-4Al alloy for nine different grain boundaries. The results were combined with a continuum dislocation pile-up model to assess the slip system level Hall-Petch slope for basal slip system (k_μ^{basal}). The results indicate that k_μ^{basal} values vary from 0.054 MPa$-$m$^{1/2}$ to 0.184 MPa$-$m$^{1/2}$.
- The k_μ^{basal} values were found to strongly correlate with the angle between the two slip plane traces on the GB plane (θ). This understanding highlights the important role of the grain boundary plane orientations in the slip system level Hall-Petch slope.
- The angle between slip directions (κ) was found to be the second most effective geometric parameter in determining the magnitude of k_μ^{basal}.
- A new equation, $k_\mu^{basal} = K^{basal}(1 - \cos(\theta)\cos(\kappa))^c$, was proposed considering both the angle between the two slip plane traces on the GB plane (θ), and the angle between slip directions (κ) to predict the slip system level Hall-Petch slope for basal slip system. This equation can be used to incorporate microstructural size effects in the crystal plasticity models.

Declaration of Competing Interest

The authors declare that they have no known competing financial interests or personal relationships that could have appeared to influence the work reported in this paper.

Acknowledgments

Data Availability: The data on which this paper was based is available in Materials Commons at doi.org/10.13011/m3-1j0q-x351 (https://materialscommons.org/public/datasets/123).

Reference

[1] J. Hirsch, T. Al-Samman, Superior light metals by texture engineering: optimized aluminum and magnesium alloys for automotive applications, Acta Mater 61 (3) (2013) 818–843.

[2] X. Wang, D. Xu, R. Wu, X. Chen, Q. Peng, L. Jin, Y. Xin, Z. Zhang, Y. Liu, X. Chen, What is going on in magnesium alloys? Journal of Materials Science & Technology 34 (2) (2018) 245–247.

[3] A. Singh, M. Nakamura, M. Watanabe, A. Kato, A. Tsai, Quasicrystal strengthened Mg–Zn–Y alloys by extrusion, Scr Mater 49 (5) (2003) 417–422.

[4] B. Wu, Y. Zhao, X. Du, Y. Zhang, F. Wagner, C. Esling, Ductility enhancement of extruded magnesium via yttrium addition, Materials Science and Engineering: A 527 (16–17) (2010) 4334–4340.

[5] S. Sandlöbes, Z. Pei, M. Friák, L.-F. Zhu, F. Wang, S. Zaefferer, D. Raabe, J. Neugebauer, Ductility improvement of Mg alloys by solid solution: ab initio modeling, synthesis and mechanical properties, Acta Mater 70 (2014) 92–104.

[6] X. Ma, Q. Jiao, L.J. Kecskes, J. El-Awady, T.P. Weihs, Effect of Basal Precipitates on Extension Twinning and Pyramidal Slip: a Micro-mechanical and Electron Microscopy Study of a Mg-Al Binary Alloy, Acta Mater (2020).

[7] J.F. Nie, Effects of precipitate shape and orientation on dispersion strengthening in magnesium alloys, Scr Mater 48 (8) (2003) 1009–1015.

[8] J.D. Robson, N. Stanford, M.R. Barnett, Effect of precipitate shape on slip and twinning in magnesium alloys, Acta Mater 59 (5) (2011) 1945–1956.

[9] H. Yu, Y. Xin, M. Wang, Q. Liu, Hall-Petch relationship in Mg alloys: a review, Journal of Materials Science & Technology 34 (2) (2018) 248–256.

[10] W. Yuan, S. Panigrahi, J.-.Q. Su, R. Mishra, Influence of grain size and texture on Hall–Petch relationship for a magnesium alloy, Scr Mater 65 (11) (2011) 994–997.

[11] J. Bohlen, M.R. Nürnberg, J.W. Senn, D. Letzig, S.R. Agnew, The texture and anisotropy of magnesium–zinc–rare earth alloy sheets, Acta Mater 55 (6) (2007) 2101–2112.

[12] N. Stanford, D. Atwell, A. Beer, C. Davies, M. Barnett, Effect of microalloying with rare-earth elements on the texture of extruded magnesium-based alloys, Scr Mater 59 (7) (2008) 772–775.

[13] R.K. Mishra, A.K. Gupta, P.R. Rao, A.K. Sachdev, A.M. Kumar, A.A. Luo, in: Influence of Cerium On Texture and Ductility of Magnesium extrusions, Essential Readings in Magnesium Technology, Springer, 2016, pp. 363–368.

[14] E. Hall, Proc. Phys. Soc, Series B 64 (1951) 747.

[15] N. Petch, The cleavage strength of polycrystals, Journal of the Iron and Steel Institute 174 (1953) 25–28.

[16] R.W. Armstrong, 60 Years of Hall-Petch: past to present nano-scale connections, Materials Transactions 55 (1) (2014) 2–12.

[17] R.W. Armstrong, Hall–Petch k dependencies in nanopolycrystals, Emerging Materials Research 3 (6) (2014) 246–251.

[18] M.D. Sangid, T. Ezaz, H. Sehitoglu, I.M. Robertson, Energy of slip transmission and nucleation at grain boundaries, Acta Mater 59 (1) (2011) 283–296.

[19] J. Han, S.L. Thomas, D.J. Srolovitz, Grain-boundary kinetics: a unified approach, Prog Mater Sci 98 (2018) 386–476.

[20] J. Wang, Atomistic simulations of dislocation pileup: grain boundaries interaction, JOM 67 (7) (2015) 1515–1525.

[21] M.D. Sangid, T. Ezaz, H. Sehitoglu, Energetics of residual dislocations associated with slip–twin and slip–GBs interactions, Materials Science and Engineering: A 542 (2012) 21–30.

[22] J. Kacher, I.M. Robertson, In situ TEM characterisation of dislocation interactions in α-titanium, Philosophical Magazine 96 (14) (2016) 1437–1447.

[23] J. Kacher, I.M. Robertson, In situ and tomographic analysis of dislocation/grain boundary interactions in α-titanium, Philosophical Magazine 94 (8) (2014) 814–829.

[24] J. Kacher, I. Robertson, Quasi-four-dimensional analysis of dislocation interactions with grain boundaries in 304 stainless steel, Acta Mater 60 (19) (2012) 6657–6672.

[25] G.J. Tucker, M.A. Tschopp, D.L. McDowell, Evolution of structure and free volume in symmetric tilt grain boundaries during dislocation nucleation, Acta Mater 58 (19) (2010) 6464–6473.

[26] M. Dewald, W. Curtin, Multiscale modelling of dislocation/grain boundary interactions. II. Screw dislocations impinging on tilt boundaries in Al, Philosophical Magazine 87 (30) (2007) 4615–4641.

[27] E. Bayerschen, A. McBride, B. Reddy, T. Böhlke, Review on slip transmission criteria in experiments and crystal plasticity models, J Mater Sci 51 (5) (2016) 2243–2258.

[28] D.E. Spearot, M.D. Sangid, Insights on slip transmission at grain boundaries from atomistic simulations, Current Opinion in Solid State and Materials Science 18 (4) (2014) 188–195.

[29] M.d. Koning, R. Miller, V. Bulatov, F.F. Abraham, Modelling grain-boundary resistance in intergranular dislocation slip transmission, Philosophical Magazine A 82 (13) (2002) 2511–2527.

[30] J. Kacher, B. Eftink, B. Cui, I. Robertson, Dislocation interactions with grain boundaries, Current Opinion in Solid State and Materials Science 18 (4) (2014) 227–243.

[31] L. Patriarca, W. Abuzaid, H. Sehitoglu, H.J. Maier, Slip transmission in bcc FeCr polycrystal, Materials science and engineering: a 588 (2013) 308–317.

[32] T. Bieler, P. Eisenlohr, C. Zhang, H. Phukan, M. Crimp, Grain boundaries and interfaces in slip transfer, Current Opinion in Solid State and Materials Science 18 (4) (2014) 212–226.

[33] A. Pineau, Crossing grain boundaries in metals by slip bands, cleavage and fatigue cracks, Philosophical Transactions of the Royal Society A: mathematical, Physical and Engineering Sciences 373 (2038) (2015) 20140131.

[34] R. Armstrong, I. Codd, R. Douthwaite, N. Petch, The plastic deformation of polycrystalline aggregates, The Philosophical Magazine: A Journal of Theoretical Experimental and Applied Physics 7 (73) (1962) 45–58.

[35] M.-.Y. Seok, I.-.C. Choi, J. Moon, S. Kim, U. Ramamurty, J.-i. Jang, Estimation of the Hall–Petch strengthening coefficient of steels through nanoindentation, Scr Mater 87 (2014) 49–52.

[36] D. Wu, J. Zhang, J. Huang, H. Bei, T.-.G. Nieh, Grain-boundary strengthening in nanocrystalline chromium and the Hall–Petch coefficient of body-centered cubic metals, Scr Mater 68 (2) (2013) 118–121.

[37] R. Armstrong, Theory of the tensile ductile-brittle behavior of poly-crystalline hcp materials, with application to beryllium, Acta Metallurgica 16 (3) (1968) 347–355.

[38] R. Yuan, I.J. Beyerlein, C. Zhou, Coupled crystal orientation-size effects on the strength of nano crystals, Sci Rep 6 (1) (2016) 1–9.

[39] H. Yu, C. Li, Y. Xin, A. Chapuis, X. Huang, Q. Liu, The mechanism for the high dependence of the Hall-Petch slope for twinning/slip on texture in Mg alloys, Acta Mater 128 (2017) 313–326.

[40] Y. Wang, C. Chang, C. Lee, H. Lin, J. Huang, Texture and weak grain size dependence in friction stir processed Mg–Al–Zn alloy, Scr Mater 55 (7) (2006) 637–640.

[41] Y. Wang, H. Choo, Influence of texture on Hall–Petch relationships in an Mg alloy, Acta Mater 81 (2014) 83–97.

[42] R.W. Armstrong, Dislocation pile-ups, material strength levels, and thermal activation, Metallurgical and Materials Transactions A 47 (12) (2016) 5801–5810.

[43] D. Wilson, J. Chapman, Effects of preferred orientation on the grain size dependence of yield strength in metals, Philosophical Magazine 8 (93) (1963) 1543–1551.

[44] B. Guan, Y. Xin, X. Huang, P. Wu, Q. Liu, Quantitative prediction of texture effect on Hall–Petch slope for magnesium alloys, Acta Mater 173 (2019) 142–152.

[45] G. Weng, A micromechanical theory of grain-size dependence in metal plasticity, J Mech Phys Solids 31 (3) (1983) 193–203.

[46] S. Sun, V. Sundararaghavan, A probabilistic crystal plasticity model for modeling grain shape effects based on slip geometry, Acta Mater 60 (13–14) (2012) 5233–5244.

[47] J. Liu, W. Xiong, A. Behera, S. Thompson, A.C. To, Mean-field polycrystal plasticity modeling with grain size and shape effects for laser additive manufactured FCC metals, Int J Solids Struct 112 (2017) 35–42.

[48] A. Singh, Y. Osawa, H. Somekawa, T. Mukai, Effect of microstructure on strength and ductility of high strength quasicrystal phase dispersed Mg–Zn–Y alloys, Materials Science and Engineering: A 611 (2014) 242–251.

[49] A.J. Wilkinson, G. Meaden, D.J. Dingley, High-resolution elastic strain measurement from electron backscatter diffraction patterns: new levels of sensitivity, Ultramicroscopy 106 (4–5) (2006) 307–313.

[50] T.B. Britton, A.J. Wilkinson, Stress fields and geometrically necessary dislocation density distributions near the head of a blocked slip band, Acta Mater 60 (16) (2012) 5773–5782.

[51] Y. Guo, T. Britton, A. Wilkinson, Slip band–grain boundary interactions in commercial-purity titanium, Acta Mater 76 (2014) 1–12.

[52] Y. Guo, D.M. Collins, E. Tarleton, F. Hofmann, A.J. Wilkinson, T.B. Britton, Dislocation density distribution at slip band-grain boundary intersections, Acta Mater 182 (2020) 172–183.

[53] D. Johnson, B. Kuhr, D. Farkas, G. Was, Quantitative analysis of localized stresses in irradiated stainless steels using high resolution electron backscatter diffraction and molecular dynamics modeling, Scr Mater 116 (2016) 87–90.

[54] D. Johnson, B. Kuhr, D. Farkas, G. Was, Quantitative Linkage between the Stress at Dislocation Channel-Grain Boundary Interaction Sites and Irradiation Assisted Stress Corrosion Crack Initiation, Acta Mater (2019).

[55] M.T. Andani, A. Lakshmanan, M. Karamooz-Ravari, V. Sundararaghavan, J. Allison, A. Misra, A quantitative study of stress fields ahead of a slip band blocked by a grain boundary in unalloyed magnesium, Sci Rep 10 (1) (2020) 1–8.

[56] BLG Vantage (http://www.hrebsd.com.).

[57] T. Britton, A. Wilkinson, High resolution electron backscatter diffraction measurements of elastic strain variations in the presence of larger lattice rotations, Ultramicroscopy 114 (2012) 82–95.

[58] M. Yaghoobi, S. Ganesan, S. Sundar, A. Lakshmanan, S. Rudraraju, J.E. Allison, V. Sundararaghavan, PRISMS-Plasticity: an open-source crystal plasticity finite element software, Computational Materials Science 169 (2019) 109078.

[59] L. Aagesen, J. Adams, J. Allison, W. Andrews, V. Araullo-Peters, T. Berman, Z. Chen, S. Daly, S. Das, S. DeWitt, Prisms: an integrated, open-source framework for accelerating predictive structural materials science, JOM 70 (10) (2018) 2298–2314.

[60] S. Ganesan, Microstructural response of magnesium alloys: 3D crystal plasticity and experimental validation, 2017.

[61] Z. Shen, R. Wagoner, W. Clark, Dislocation and grain boundary interactions in metals, Acta metall 36 (12) (1988) 3231–3242.

[62] L.T. Hansen, D.T. Fullwood, E.R. Homer, R.H. Wagoner, H. Lim, J.D. Carroll, G. Zhou, H.J. Bong, An investigation of geometrically necessary dislocations and back stress in large grained tantalum via EBSD and CPFEM, Materials Science and Engineering: A 772 (2020) 138704.

[63] A. Akhtar, E. Teghtsoonian, Substitutional solution hardening of magnesium single crystals, Philosophical Magazine 25 (4) (1972) 897–916.

[64] A. Githens, S. Ganesan, Z. Chen, J. Allison, V. Sundararaghavan, S. Daly, Characterizing microscale deformation mechanisms and macroscopic tensile properties of a high strength magnesium rare-earth alloy: a combined experimental and crystal plasticity approach, Acta Mater 186 (2020) 77–94.

[65] K.G. Davis, Slip Continuity Across Grain Boundaries in Aluminum, University of British Columbia, 1959.

[66] C. Brandl, E. Bitzek, P. Derlet, H. Van Swygenhoven, Slip transfer through a general high angle grain boundary in nanocrystalline aluminum, Appl Phys Lett 91 (11) (2007) 111914.

[67] I. Beyerlein, N. Mara, J. Wang, J. Carpenter, S. Zheng, W. Han, R. Zhang, K. Kang, T. Nizolek, T. Pollock, Structure–property–functionality of bimetal interfaces, Jom 64 (10) (2012) 1192–1207.

[68] W. Bollmann, Crystal defects and crystalline interfaces, Springer Science & Business Media 2012.

[69] L. Lim, R. Raj, The role of residual dislocation arrays in slip induced cavitation, migration and dynamic recrystallization at grain boundaries, Acta Metallurgica 33 (12) (1985) 2205–2214.

[70] M. Marcinkowski, W.F. Tseng, Dislocation behavior at tilt boundaries of infinite extent, Metallurgical Transactions 1 (12) (1970) 3397–3401.

[71] T. Lee, I. Robertson, H. Birnbaum, AnIn Situ transmission electron microscope deformation study of the slip transfer mechanisms in metals, Metallurgical Transactions A 21 (9) (1990) 2437–2447.

[72] Z. Shen, R. Wagoner, W. Clark, Dislocation pile-up and grain boundary interactions in 304 stainless steel, Scripta metallurgica 20 (6) (1986) 921–926.

[73] T. Lee, I. Robertson, H. Birnbaum, TEM in situ deformation study of the interaction of lattice dislocations with grain boundaries in metals, Philosophical Magazine A 62 (1) (1990) 131–153.

[74] H. Lim, M. Lee, J. Kim, B. Adams, R. Wagoner, Simulation of polycrystal deformation with grain and grain boundary effects, International Journal of Plasticity 27 (9) (2011) 1328–1354.

[75] J.P. Hirth, J. Lothe, T. Mura, Theory of dislocations, American Society of Mechanical Engineers Digital Collection (1983).

[76] Y. Guo, Exploration of Microstructure Related Deformation Gradients in Commercial Purity Titanium, The University of Oxford, 2015.

[77] E. Deda, T.D. Berman, J.E. Allison, The influence of Al content and thickness on the microstructure and tensile properties in high-pressure die cast magnesium alloys, Metallurgical and Materials Transactions A 48 (4) (2017) 1999–2014.

[78] R. Ramprasad, R. Batra, G. Pilania, A. Mannodi-Kanakkithodi, C. Kim, Machine learning in materials informatics: recent applications and prospects, npj Computational Materials 3 (1) (2017) 1–13.